Title:

Influence of print paths on mechanical properties and fracture propagation of 3D printed concrete

Author names:

Kota NAKASE[*1], Katsufumi HASHIMOTO[*2], Takafumi SUGIYAMA[*3], Katsuya KONO[*4, 5]

Author affiliations:

[1] Environmental Material Engineering Laboratory, Division of Field Engineering for the Environment, Graduate School of Engineering, Hokkaido University, A4-53, N13W8, Sapporo, 060-8628, Japan, k0utao121@eis.hokudai.ac.jp, **corresponding author**

[2] Environmental Material Engineering Laboratory, Division of Civil Engineering, Faculty of Engineering, Hokkaido University, A4-08, N13W8, Sapporo, 060-8628, Japan, hashimoto.k@eng.hokudai.ac.jp

[3] Environmental Material Engineering Laboratory, Division of Civil Engineering, Faculty of Engineering, Hokkaido University, A4-07, N13W8, Sapporo, 060-8628, Japan, takaf@eng.hokudai.ac.jp

[4] Nghi Son Cement Corporation, 23 Phan Chu Trinh, Hoan Kiem, Hanoi, Vietnam, kono@nghison.com.vn

[5] Taiheiyo Cement Corporation Research Center, 2-4-2, Osaku, Sakura City, Chiba, 285-8655, Japan, katsuya_kono@taiheiyo-cement.co.jp

Abstract: here is the abstract (200 words)

When constructing concrete structures using 3D printing, it is important to consider the anisotropy due to the printing process. The print path influences the formation of layer interfaces and inter-filament voids, and the fracture propagation behavior of the printed specimen. In this paper, the fracture propagation behavior of printed mortar specimens under compressive, tensile, and bending stresses is evaluated for different print paths. X-ray computed tomography visualizes the interior of printed specimens and shows that the pressure during material extrusion elongates the intra-filament voids. The inter-filament void structure is influenced by the print path, forming an aligned structure in one direction or a complex lattice-like structure. Anisotropy in the deformation direction under compressive stress, which is influenced by the inter-filament void structure, is assessed by 3D scanning. Under tensile stress, Digital Image Correlation (DIC) visualizes that tensile stress is concentrated in the layer interface, causing cracks to propagate along the layer interface. Under bending stress, DIC evaluates the effect of the print path on fracture propagation behavior. The results show that the mechanical properties and fracture propagation behavior of printed specimens are affected by the arrangement of the layer interface and inter-filament void, which is governed by the print path. (200 words)

Keywords:
3D concrete printing; print path; mechanical properties; layer interface; inter-filament void

1 Introduction

3D concrete printing (3DCP), an additive manufacturing technology using cementitious materials as extrusion material for large-scale structures, has been developed and has received much technical and research interest recently [1–5]. There are several methods of 3D printing technology such as binder jetting, material extrusion, material jetting, energy deposition, powder bed fusion, sheet lamination and vat photopolymerization [6]. Currently, the material extrusion method is mainly introduced for 3DCP [7,8], in which the material with shape stability and form buildability is extruded and printed (deposited) by controlling nozzle based on 3D CAD data (geometrical information for printing design). In the conventional concrete casting method, the material is uniformly filled into simple shape formwork and compacted appropriately. On the other hand, 3DCP allows the material to be extruded and printed directly into the three-dimensional space without formwork. It is expected to increase the flexibility of design shape [2,9]. Since 3DCP uses a larger amount of cement than conventional cast concrete [10], studies have been conducted on the use of supplementary cementitious materials for layered filament (material extruded in the form of strings) to improve the sustainability of 3DCP [10,11]. 3DCP could reduce the environmental impact by the combination of sufficiently planning the material usage and the structural design [4,9,10,12]. The research achievements in laboratory tests are now applied for several construction sites in real situations [13,14], and the various studies including the installation of reinforcement materials are challengingly conducted to further increase the number of case examples to build 3D printed concrete structures [3].

In 3DCP, it is considered that the structural behavior is potentially altered due to the printing process [15–17]. The previous research related to 3DCP has mainly focused on the requirement for material extrusion, the formation and properties of layer interface and the mechanical properties of 3D printed concrete [1].

Cementitious materials used as the printing materials must have appropriate extrudability to prevent blockage inside the nozzle [18,19]. In addition, they are required to have the buildability during printing so that it prevents collapse with excessive deformation and settlement [20,21]. Many studies have been conducted related to the rheological properties required in the fresh state of such filament as 3D printing component under development of shear strength against gravity-induced stress [21–24]. In the material extrusion phase, the optimized nozzle geometry has been tried to reduce the extrusion resistance in a round-shaped nozzle by removing the extra die to avoid additional friction [25].

The filament adhesion is a major concern during the process of depositing the extruded material layer by layer. It shows unstable adhesion such as cold joints depending on the printing time interval and the filament surface condition [5,16,26]. The properties of the layer interface have been frequently analyzed regarding the printing parameters and the void structure in the layer interface region to understand the deformation mechanism [15,27]. The properties of the layer interface have been investigated mainly for the void structure of the interfacial region using X-ray computed tomography (X-ray CT) [28–31]. Several approaches have been proposed to improve adhesion at the layer interface of 3D printed concrete [32,33].

The mechanical properties of 3D printed concrete after hardening are also one of the main research topics of its structural capacity. Most of the research achievements on structural performance and fracture mechanism of 3D printed concrete have indicated that there is anisotropy in the mechanical properties of 3D printed concrete [16,23,34–38]. Many studies have pointed out that the rheological properties of the extruded material in the fresh state (yield stress, plastic viscosity and so forth) and printing parameters (nozzle shape, printing speed, time interval and so forth) play an important role in the hardened mechanical properties of 3DCP.

In contrast to conventionally cast concrete, the mechanical properties of 3D printed concrete are affected by the layer interface formed by the printing process [39]. The print path is known as an infill pattern in commonly used resin 3D printers, and it is an important printing parameter in the quality of object modeling [40]. Nevertheless, printing parameters that have been focused on in previous studies of 3DCP are often the printing time interval and the nozzle geometry [23,35]. It indicates that there are few studies found to consider the effects of differences in the printing direction and the print path pattern on mechanical properties and fracture behavior of 3D printed concrete except in a few literatures [41–43]. In one literature [41], the print path is varied in the horizontal plane into the reciprocating path (path1) and the rotary path (path2). However, printed specimens are printed by a repetition of only path1 or a repetition of only path2, which are the same printing path in the vertical direction. In the other literatures, the printing direction in a reciprocating path is varied to 0°, 45°, 90°, 135° [42] or 0°, 90° [43] with alternating the printed layers, resulted in changing the printing path not only in the horizontal direction but also in the vertical direction. However, while the overall anisotropic mechanical properties of the printed specimen under compression and shear loading have been evaluated, the effect of the print path on the fracture propagation behavior has not been evaluated [42]. Alternatively, the fracture propagation is evaluated by only acoustic emission [43]. Since the print path is a printing parameter related to the layer interface placement, its effect on the formation of inter-filament void structures in 3D printed concrete and that on the deformation behavior needs to be investigated in more detail.

3DCP allows the cement-based materials to be extruded and built freely when the design data is fabricated in three-dimensional space. Consequently, it is expected to be combined with topology optimization methods in effectively determining and constructing the most appropriate structural member [44]. Topology optimization is a mathematical method to determine the structural form that maximizes the desired performance under certain constraints such as load and boundary conditions with mass and volume limits. When printing the optimal structure determined by this mathematical method, the print path can be set at possible directions and patterns. In other words, in addition to optimizing the structural morphology, it is necessary to determine the optimal print path considering the anisotropy of mechanical properties and structural capacities [45].

In order to further investigate the mechanical properties of 3D printed concrete and to develop the construction technology taking advantage of the high design freedom of 3DCP in combination with topology optimization, it is necessary to evaluate the effect of the print path on the mechanical properties and the fracture propagation behavior of 3D printed concrete. This paper aims to investigate the influence of print paths on the mechanical properties of 3D printed concrete. For this purpose, the fracture propagation behaviors under compressive, tensile and bending stresses were evaluated by means of non-destructive testing methods. In the case of applying compressive loading, X-ray CT and 3D scanning were introduced before and after loading to evaluate the effects of printing direction on the internal crack propagation and the surface deformation distribution. As for the cases of applying tensile and bending loading, the influence of print paths on fracture propagation behavior was evaluated by digital image correlation (DIC) with identifying the strain distribution in the cross-section of 3D printed concrete.

2. Materials and methods

2.1. 3D printed specimen preparation

2.1.1. Material properties

Table 1 shows the mix proportions. In this study, the binder (B) is the pre-mixed powder consisting of Ordinary Portland Cement (OPC) and silica fume. The fine aggregate (S) is silica sand (2.58g/cm^3, F.M. of 1.73). This proportion is designed to meet the material requirements of 3DCP, such as extrudability and buildability. Water to binder ratio (W/B) is 20%, and 1.6 (mass% to B) polycarboxylate-based superplasticizer (SP) is added.

Table 1 Mix proportions

W/B (%)	W (kg/m^3)	B (kg/m^3)	S (kg/m^3)	SP (mass% to B)
20	217	1085	1085	1.6

It was confirmed that the air content after mixing was 7.1%, and the mortar flow value obtained by mortar flow testing according to JIS R5201 was 149 mm. Fig. 1 shows the mortar flow testing as specified in JIS R5201. After filling the flow cone with mortar, the flow table is immediately dropped 15 times within 15 seconds. The diameter of the mortar is measured to obtain the flow value. The 28d strength of the cast specimen made with the same materials mix proportion was 88.0 N/mm^2.

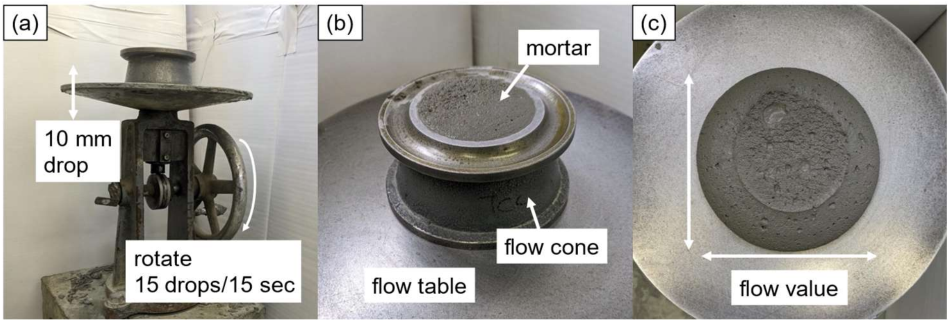

Fig. 1 Mortar floe testing: (a) Overview of the testing machine, (b) Cast mortar into the flow cone and (c) Measure the flow value after 15 drops/ 15sec.

2.1.2. Print condition and print path

The printed specimen was prepared using the material extrusion 3D printer shown in Fig. 2. As shown in the figure, a bottle-shaped cartridge is filled with mortar and fixed to the printer.

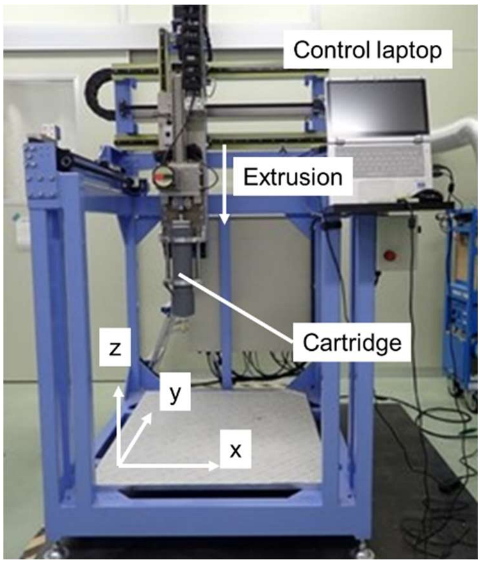

Fig. 2 Material extrusion 3D printer.

Circular or rectangular [20] nozzle outlet shapes are often employed, and the circular nozzle outlet shape was also employed in this study with setting the nozzle inner diameter at 14 mm, where the nozzle extrusion width was 16 mm for the printer used. Each layer height for the 3D printed specimen was set at 10 mm and the number of layers after printing at 12 with the nozzle moving speed of 30 mm/s.

Fig. 3 shows the print paths considered for approximately 100 x 100 x 400 mm prism specimens in this paper. In pattern (I), the layers are printed in the circumferential direction. In pattern (II), the layers are printed in the long side direction. In pattern (III), the layers are printed in the short side direction. In patterns (I), (II) and (III), the printed specimen is fabricated, repeatedly printing the same layers in each layer. In pattern (IV), the odd-numbered layers from bottom are printed in the long side direction as in pattern (II) and the even-numbered layers from bottom are printed in the short side direction as in pattern (III). Namely, in pattern (IV), the printed specimen is prepared by printing each layer in orthogonal directions for the odd-numbered layer and even-numbered layer.

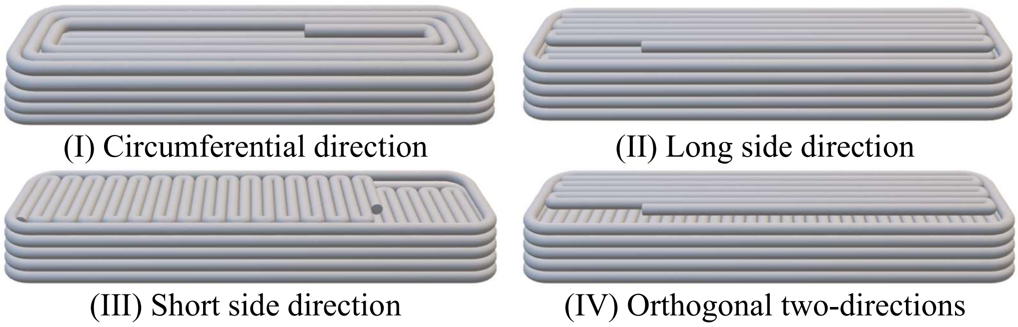

Fig. 3 Print path.

Fig. 4 shows an overview of the cylindrical and the prismatic specimens obtained from the printed specimen by coring and slicing respectively. Previous studies have also obtained cylindrical and prismatic specimens from printed specimens by coring [16,28] and slicing [26,36]. Three cylindrical specimens (φ45 x 90 mm) and two prismatic specimens (40 x 40 x 160 mm) were prepared for the following experiment and measurement. In above-mentioned printing patterns, the outermost layer was circumferentially printed in order to improve the stability of the printed specimen during fabrication. The cylinder and the prismatic specimens were obtained from positions with excluding the outermost layer.

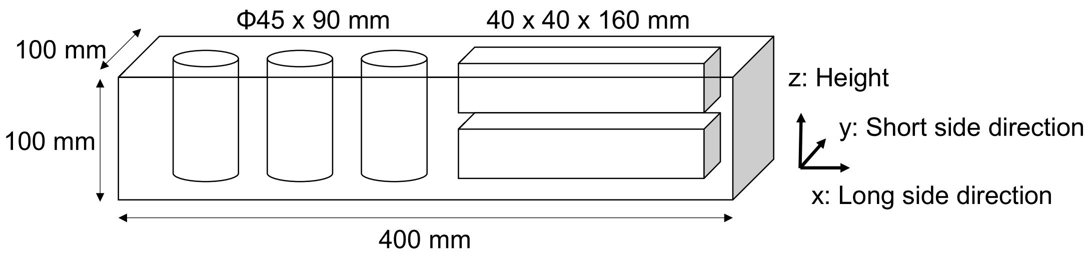

Fig. 4 Overview of preparation for cylindrical and prismatic specimens.

2.2. Experimental method

Compressive, split tensile and bending tests were conducted on the obtained cylindrical/prismatic specimens at nine months after printing which is a sufficiently long curing period [46]. Fig. 5 shows an outline of the loading tests in this study.

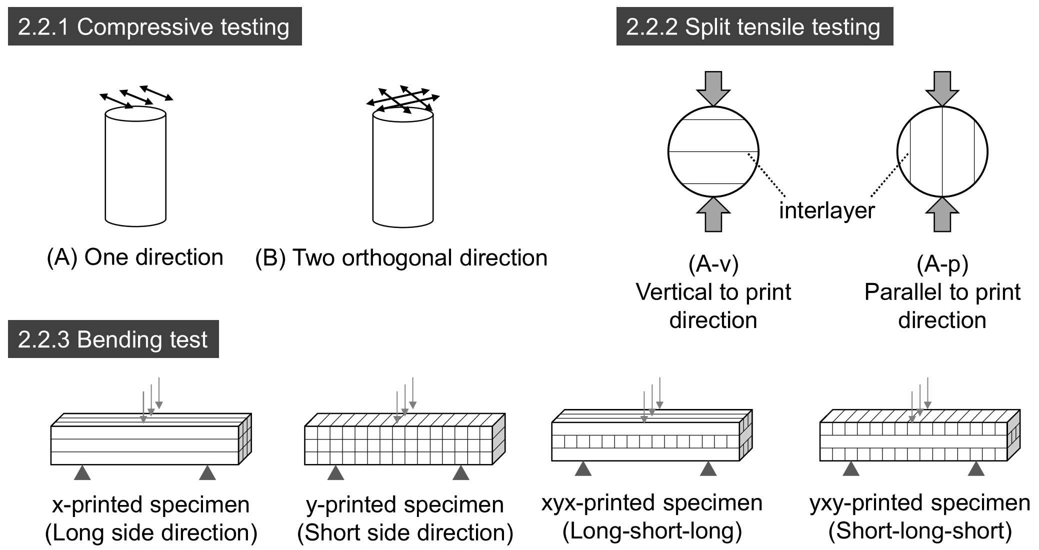

Fig.5 Outline of the loading tests.

In the cylindrical specimens, pattern (I), (II) and (III) are printed in the circumferential, long side and short side directions respectively in all layers. Hence, in the obtained cylindrical specimens, pattern (I), (II) and (III) can be regarded as printed specimens with the same print direction in rotating the specimens by 90 degrees. In other words, there are two conditions of the print paths to be considered for the cylinder specimen, i.e. condition (A): all layers are printed in one direction (pattern (I), (II) and (III)) and condition (B): alternately printed in orthogonal two-directions (pattern (IV)).

For the prismatic specimens, the specimens printed in the long side direction were obtained from pattern (I) and (II), and the specimens printed in the short side direction were obtained from pattern (III). From pattern (IV), the specimens with bottom and top layers printed in the long (short) side direction and the middle layer printed in the short (long) side direction were obtained.

As described in Fig. 4, the x, y and z-axis were respectively set in the long side, the short side direction and the height direction. Therefore, all prismatic specimens can be classified into the following four types as illustrated in Fig. 5: x-printed specimens printed only in the long side direction, y-printed specimens printed only in the short side direction, xyx-printed specimens printed in the order of long-short-long side direction and yxy-printed specimen printed in the order of short-long-short side direction.

2.2.1. Compressive test

It is important to understand the mechanical properties of concrete, which is expected to be in use under compressive stress to enable efficient design of 3DCP components and structures. Compression test was performed on the cylindrical specimens obtained from the printed specimens. The effect of print path on the mechanical properties of 3D-printed concrete under compressive stress was evaluated.

The top and bottom end of the cylindrical specimens were capped with gypsum to consider interlayer irregularities on the surfaces. This allowed cracks to be introduced by compressive loading without unintentional stress localization. The loading rate was set at 5.0 N/mm^2/min. Loading was stopped when cracks were visually observed on the specimen surface with drop of loading to conduct X-ray CT after loading to visualize the internal crack propagations. Compressive tests were conducted on three specimens each for both printing conditions (A) and (B) referred to Fig. 5 in 2.2.1.

2.2.2. Split tensile test

In 3DCP, adhesion between each layer is an important parameter for the strength of the printed concrete [15,16,35,47,48]. Previous studies have pointed out the anisotropy of tensile strength in tensile tests depending on the direction of printing and loading. The tensile strength is significantly lower when tensile force is applied in the direction perpendicular to the printing direction compared to when tensile force is applied in the printing direction. It indicates that the bond strength at the layer interface is much smaller than when tensile force is applied to the filament cross-section. This allows us to evaluate the bond strength at the layer interface and the anisotropy of the tensile strength of the 3D printed concrete. Tensile testing has been investigated using various methods [5], such as direct tension test and splitting test. In this paper, the effect of the print direction under tensile stress was also examined by split tensile test.

Split tensile tests were conducted on the cylindrical specimens (φ45 x 90 mm) of condition (A), which were obtained by core sampling from the printed specimens in Fig. 4 in 2.2.1. To evaluate the effect of the layer interface on adhesion between filaments, the specimens were loaded in the following two directions: the direction vertical to the print direction (condition (A-v) in Fig. 5), and the direction parallel to the print direction (condition (A-p) in Fig. 5). The loading speed was controlled at 0.2 mm/min for the displacement at middle of the specimen. Tensile strength was calculated by the following Eq. (1).

$$f_t = \frac{2P}{\pi d l} \quad (1)$$

Here, ft: tensile strength [N/mm^2], P: maximum load [N], d: specimen diameter [mm], l: specimen height [mm]

Three split tensile tests were conducted on the cast specimens for comparison in fracture behavior with 3D printed specimen, and two of the specimens were tested for each of the conditions (A-v) and (A-p).

2.2.3. Bending test

As shown in Fig. 5 in 2.2.1, three-point bending tests by loading were conducted on the prismatic specimen (40 x 40 x 160 mm) cut from printed specimen. The loading rate was controlled at 3.0 kN/min. Similarly to the compressive test, the top and bottom surfaces were smoothed with gypsum in order to avoid stress localization. Bending strength was calculated by the following Eq. (2).

$$f_{\mathrm{b}}=\frac{3PL}{2bh^2} \tag{2}$$

Here, *fb*: bending strength [N/mm^2], *P*: maximum load [N], *L*: span [mm], *b*: width of fracture section [mm], *h*: height of fracture section [mm]

For the bending tests, two samples for the cast specimens, two samples for y-printed specimens and three samples for x-printed specimens were tested. xyx-printed specimen and yxy-printed specimen were tested for one sample each.

2.2.4. X-ray computed tomography (X-ray CT)

X-ray CT was used to observe the internal structure and internal crack propagation of cast specimens and printed specimens. In X-ray CT, X-ray irradiated from the X-ray source before and after transmission through the object is detected and the X-ray attenuation ratio in the target material is visualized. The stage is rotated during imaging to transmit X-rays from all directions. The acquired data is reconstructed by computer to obtain a series of cross-sectional images.

In the field of concrete engineering, X-ray CT is used to visualize internal cracks and quantify the internal void structure [49,50]. In 3DCP, it has been used in studies on evaluating the void structure at the layer interface [30] and the relationship between the void structure at the layer interface and layer adhesion [28].

Since the X-ray absorption coefficient of an object depends on its density, the acquired cross-sectional image sequence shows density distribution in the targeted solid. As for X-ray CT images in this paper, the areas with small (dark) grayscale values represent low densities, such as air (voids and air bubbles) and cracks. On the other hand, the areas with relatively high (bright) grayscale values represent cement paste and aggregate.

During image detection process, 0.2 mm thickness Cu filter was used to remove low-energy X-rays and reduce artifacts in the obtained images. By the above imaging process, a cross-sectional image sequence with a resolution of 24.86 μm/pixel and an image size of 2864 x 2864 pixels was captured.

2.2.5. 3D scanning

In this paper, 3D scanning measurements and analysis were conducted to evaluate the effect of the print path on three-dimensional deformation under compressive stress. It is known that the mechanical properties of printed specimens are anisotropic, depending on the layered structure resulting from the printing process [16,34,35]. However, there are few investigation examples of evaluating the effect of the print path on the deformation of printed specimens. When evaluating the deformation of structural members due to loading, a strain gauge is commonly used by attaching to the surface for measuring local deformation at a specific point. However, evaluation of local deformation at specific surface locations is insufficient to clearly identify the anisotropic behavior, which three-dimensionally and randomly occurs on the target body surface of 3D printed concrete.

In some experimental cases of previous studies, the deformation is evaluated as a distribution based on point cloud data obtained by 3D scanning before and after loading [51]. This method is widely used in reverse engineering. Scanning an existing product, its structure with geometrical information is analyzed, so that it is reproduced using 3D printing technology. The 3D scanning technique is often used for inspection of structural form. In 3DCP, 3D scanning is an evaluation method to check the quality of printing construction by comparing the design data with the printed specimen [52]. Although there are some practical achievements using this technique to evaluate the surface shape of the material after extrusion [22], there are no examples of evaluating deformation due to loading for 3D printed concrete.

Fig. 6 shows the 3D scanning process and the technical procedure. A white light 3D scanner was used with the resolution (point-to-point pitch) of 0.17 mm to 0.2 mm and the one-shot accuracy of 0.1 mm. The 3D scanner introduces a non-contact light projection method using white light LED as light source. The light source on the scanner irradiates some patterned lights onto the object, and the camera captures the pattern reflected from the object surface unevenness to acquire three-dimensional coordinate data of the object surface. The three-dimensional coordinates of the object surface can be obtained by rotating the object during measurement. In order to capture and scan the whole surface of the specimen, which is covered from all directions, multiple scans were carried out by changing the position of the specimen until acquiring the enough amount of point cloud data for surface shape.

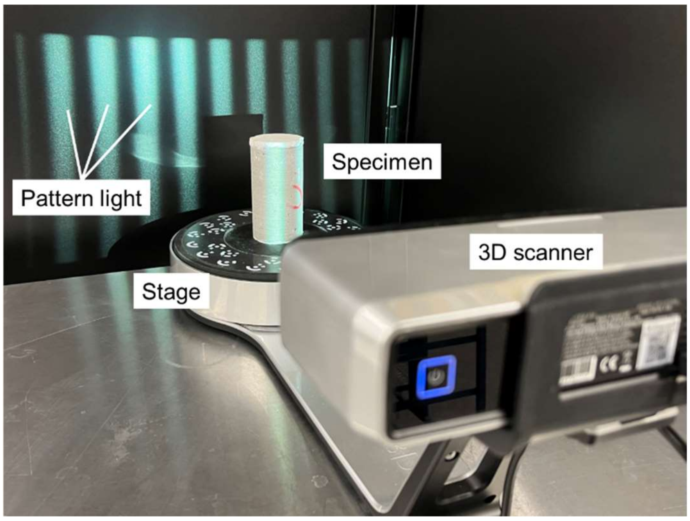

Fig. 6 Setup for 3D scanning.

After scanning, the obtained point cloud data were combined and converted to polygon data to analyze the three-dimensional deformation. In any polygon data, the number of vertices was around 55,000, and that of faces was 100,000. The shortest distance from each vertex of the polygon data before loading to each vertex of the polygon data after loading was calculated. This distance was defined as the value of deformation (δ) due to loading. In order to distinctly observe and emphasize the deformation due to loading, the deformation due to compression loading was evaluated using Eq. (3).

$$\left(x_{\mathrm{plot}}, y_{\mathrm{plot}}\right) = (x, y) + \frac{|\delta|}{\delta_{max}}(x, y) \tag{3}$$

Here, δ: the shortest distance to each vertex before and after loading, δmax: the maximum value of δ over the entire specimen

After loading, the cylindrical specimen could be partially defective due to the compressive loading. However, since the defects are the result of out-of-plane deformation due to loading, only the magnitude of δ in Eq. (3) is considered and its sign is not considered. It means that the difference in the positive/negative sign of δ is indicated by the red line when δ in Eq. (3) is positive and the blue line when δ is negative.

2.2.6. Digital Image Correlation (DIC)

This paper evaluates the effects of different print paths, i.e. different layer interfaces and inter-filament void structures, on fracture propagation behavior by digital image correlation (DIC) during the split tensile test and the bending test. DIC measures the deformation of the object surface by capturing and combining the deformation of a small subset [53].

DIC can evaluate the strain distribution on the specimen surface over time by capturing the random pattern applied to the specimen surface as it changes during loading. In 3DCP, this method has been also used to evaluate the fracture propagation initiation from the layer interface [36,43]. In this paper, specimens obtained by cutting from the printed specimens were used in the bending tests. Following the fabrication procedure, the layer interfaces and inter-filament voids, which are normally located inside the print, can be identified on the surface of the specimen. As a result, the analysis with DIC can visualize the fracture propagation behavior inside the printed specimen.

Fig. 7 shows the overview of DIC process in this study. Tensile and flexural fractures examined in this paper include the brittle fractures that are completed instantaneously. In order to evaluate the influence of layer interface and inter-filament void on the fracture propagation behavior, a high-speed camera was used with image shooting speed of 4000 fps and camera shutter speed of 1/20000 sec. The high-speed camera recorded continuously and acquired image sequences for approximately 1.5 seconds before and after the failure phase. The image size was 1024 x 512 pixels with a resolution of 0.105 mm/pixel.

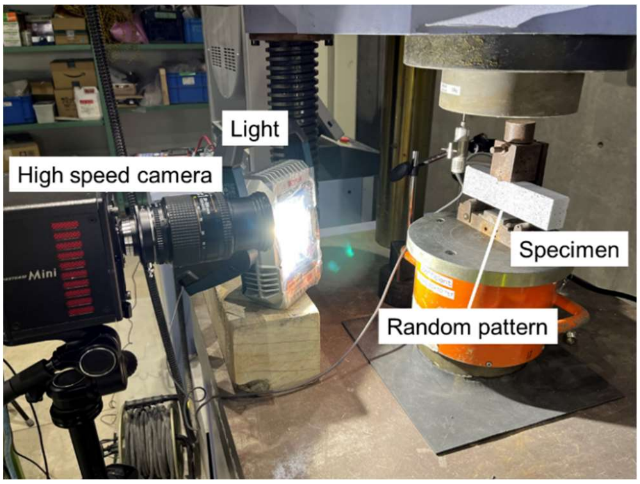

Fig. 7 Setup for Digital Image Correlation (DIC).

3. Results and discussion

3.1. Results of compressive test

Fig. 8 shows the cross-sectional and longitudinal X-ray CT images of the cast specimens and the printed specimens after internal cracks were introduced by compressive loading. The yellow lines indicate the positions of the corresponding cross-sections in vertical and horizontal directions. The stress value applied for the crack introduction is shown at the top left of each image.

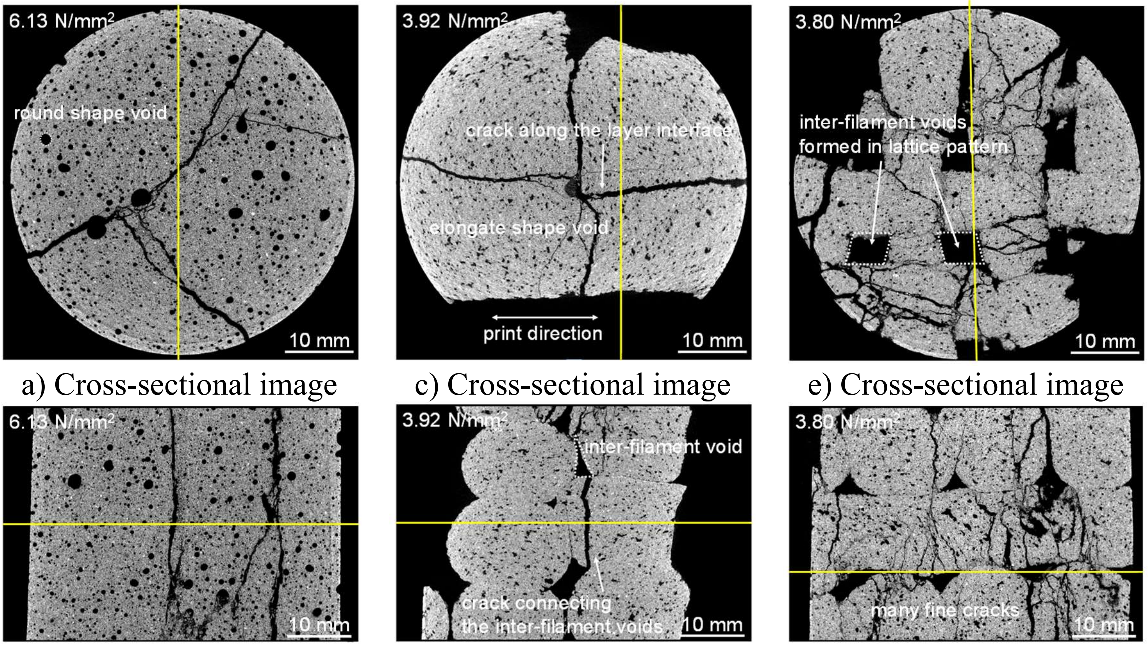

a) Cross-sectional image; c) Cross-sectional image; e) Cross-sectional image

b) Longitudinal image; d) Longitudinal image; f) Longitudinal image

Cast specimen; (A): One direction; (B): Orthogonal two-direction

Fig. 8 X-ray CT images.

3.1.1. Void structure

As shown in Fig. 8a) and b), the voids in the cast specimens are rounded in shape. In contrast, the printed specimens shown in Fig. 8c) to f) have elongated shape intra-filament voids. Intra-filament void is the void formed inside the extruded filament, whereas inter-filament void is the void formed between the deposited filaments [40]. This indicates that the pressure during extrusion causes the intra-filament void to elongate in the material flow direction. This has been also reported in previous studies [30,36,47], and a detailed evaluation on voids distribution and their shape has been conducted. Namely, as for 3D printed concrete, the voids are observed to be consistently elongated in the vertical extrusion direction and flattened in the vertical direction for layer arrangement. In contrast, cast concrete has similar dimensions in the plane (xy-plane) but is pressed in the casting direction (z-direction) [30,47]. In conventional cast concrete, it has been pointed out that the void structure inside the concrete, i.e. its size, geometry and distribution, is closely related to its mechanical properties [54–56]. The change in void shape is considered to affect the durability of printed specimens [57,58] as well as the propagation of cracks and degradation of mechanical properties [47]. The inter-filament voids in the interlayer zones allow faster water transport in the interlayer zones of 3D printed concrete compared to cast concrete [58]. The void characteristics could be an important parameter in the durability evaluation of printed specimens.

3.1.2. Internal crack propagation

As shown in Fig. 8a) and b), in the cast specimen, the cracks propagate randomly. As for condition (A) shown in Fig. 8c) and d), the printing direction is in the left to right directions in the cross-sectional image. Displayed in the longitudinal cross-sectional image, the cracks propagate regularly with connecting the inter-filament voids. In addition, two large cracks are observed in the left-right direction of the cross-sectional image along the layer interface and in the direction perpendicular to it. In contrast, as for condition (B) shown in Fig. 8e) and f), many micro cracks are observed throughout the image in both transverse and longitudinal directions. These results indicate that the crack propagation under compressive stress is altered with depending on the change in the print path.

Fig. 9 shows 3D and projection images of inter-filament voids extracted from the X-ray CT images of the specimen before loading. The air space in this image corresponds to the internal void networks surrounded by filaments inside the printed specimen. The x, y and z projections are projection onto the y-z, x-z and x-y planes, respectively. The grey scale in the projection image shows the average of all voxel values for each stacked y-z (x-z, x-y) point.

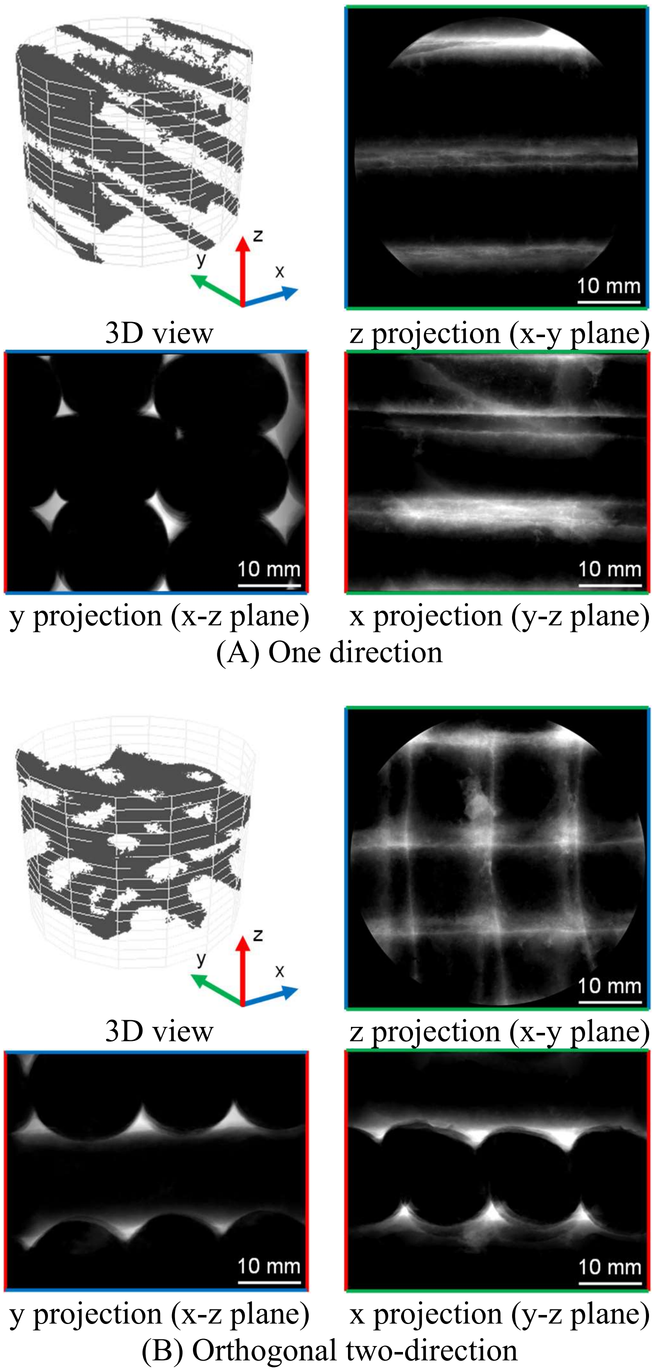

Fig. 9 3D and projection image of inter-filament void structure.

In condition (A), in the specimen where the layers are printed in one direction, the inter-filament voids are also aligned in one direction shown in 3D view and z projection. The y projection shows the cross-section of filament and inter-filament voids. The inter-filament voids are diamond shaped and surrounded by filaments. On the other hand, in condition (B), in the specimen where the layers are printed in orthogonal two-directions, the 3D view and z projection show that the complex lattice-like inter-filament void structure is formed. From the y and x projections, it can be seen that the middle layer is printed orthogonally to the top and bottom layers in this region of interest (ROI). The inter-filament void in condition B is triangle shaped.

The volume fraction of inter-filament void to ROI is 5.42% and 4.91% for conditions A and B respectively, which is not a significant difference. However, in condition (B) as shown in Fig. 8e), inter-filament voids are distributed within the printed specimen. It can be inferred that the cracks are not localized due to complex stress transfer in condition (B) compared to condition (A), resulting in the generation of micro crack distribution.

3.1.3. Deformation distribution

The effect of the print path on the deformation during compression failure was evaluated by using the deformation δ (see Eq. (3)) calculated from polygonal data of the cylinder specimen surface obtained before and after loading, combined with cross-sectional images obtained by the X-ray CT method. Fig. 10 displays the deformation in the cross-section at 5 mm, 25 mm, 45 mm and 65 mm from the bottom of the specimen under conditions (A) and (B). The white lines in the figures are the coordinates of the specimen surface before loading (x-y coordinates at z=5mm, 25mm, 45mm and 65mm). The red and blue lines in the figure show the deformation due to loading calculated by Eq. (3) (see 2.2.5.).

In the figures of Fig. 10, since some surface polygon data for body of specimens is lost and non-detectable due to loading, the deformation is not correctly shown based on the scanning after loading.

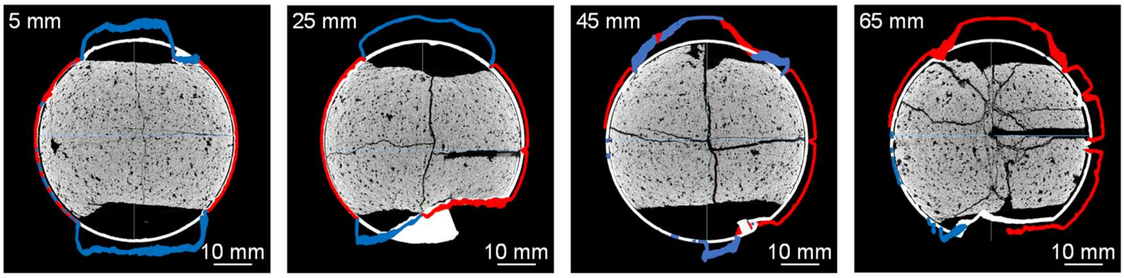

(A) One direction

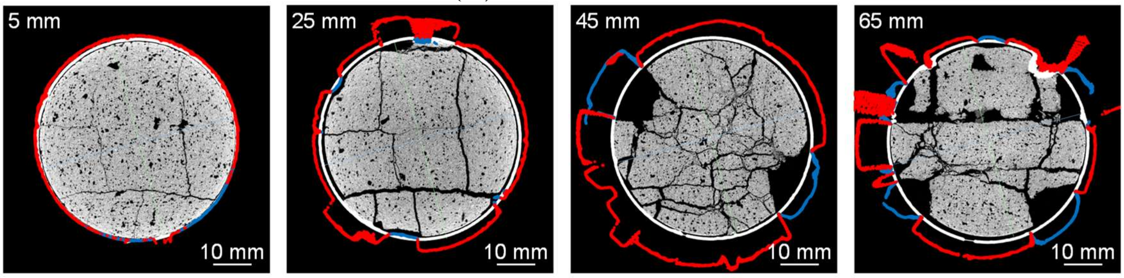

(B) Orthogonal two-directions

Fig. 10 Deformation in each cross-section due to compressive loading.

In addition to the anisotropy in the strength of printed specimens due to the relationship between the printing direction and the loading directions shown in previous studies [16], anisotropy in the deformation direction of the printed specimen can be also observed. In condition (A), where the specimens were printed in only one direction, the printing direction is in the left and right directions of the cross-sectional image in Fig. 10. However, the printed specimen deformed markedly in the direction perpendicular to the printing direction. In condition (B), where the specimens are printed in orthogonal two-directions, the deformation is found in all directions. Anisotropy in the deformation direction observed in condition (A) cannot be confirmed for the entire cross-section. It implies that the inter-filament void structure changed with depending on the print path. This is because the anisotropy of deformation disappears due to the complex lattice distribution of the inter-filament voids governing crack propagation in the condition (B) specimen. 3D scanning revealed that the printing path affects not only crack propagation but also deformation, resulting in anisotropy of the deformation direction.

3.2. Results of split tensile test

3.2.1. Split tensile strength

Fig. 11 shows the tensile strength of the cast specimens and the printed specimens obtained from split tensile tests. The coefficient of variation of tensile strength of cast specimen, condition (A-v) and condition (A-p) are 0.434, 0.003 and 0.127 respectively. The tensile strength of condition (A-v), loaded perpendicular to the printing direction, is slightly lower than that of the cast specimen. On the other hand, the tensile strength of the printed specimens under condition (A-p), where the load is parallel to the printing direction, is significantly lower than that of the cast specimens and condition (A-v). Accordingly, it can be clearly confirmed that the printing direction is responsible for the anisotropy in the mechanical performance of the printed specimen under tensile stress. Previous studies have shown that tensile strength (interlayer bond strength) decreases at the layer interface, and the effects of printing time interval and filament surface condition on tensile strength (interlayer bond strength) have been investigated [26,28,48]. In this study, fracture propagation behavior at the layer interface zone was evaluated by DIC.

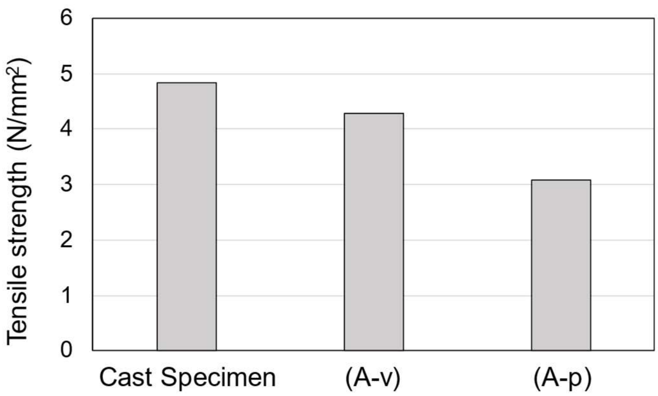

Fig. 11 Tensile strength.

3.2.2. Fracture propagation

Fig. 12 shows the principal strain distribution images obtained by DIC during the split tensile test 0.00025 seconds before cracking i.e., one frame before cracking (left) and at crack initiation (right). The layer interface is indicated by white dotted lines in Fig. 11b) and c).

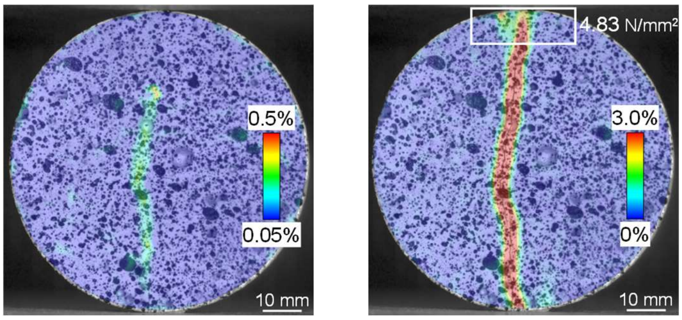

0.00025 sec before cracking Cracking

a) Cast specimen

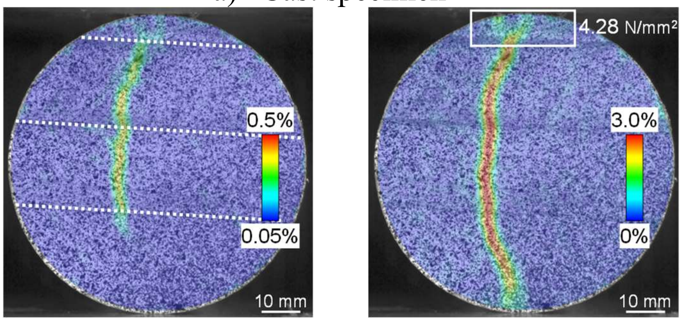

0.00025 sec before cracking Cracking

b) (A-v): Loading vertically to the printing direction

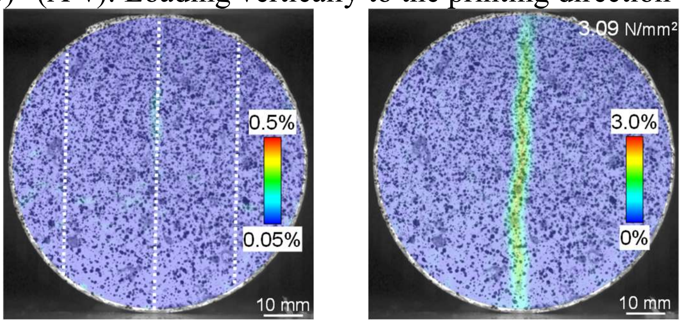

0.00025 sec before cracking Cracking

c) (A-p): Loading parallel to the printing direction

Fig. 12 Principal strain distribution by DIC.

In all the cases, the crack is formed at the center of the cross-section, where the tensile stress is concentrated in the cross-section. In the area near the loading surface, which is rectangularly circled by white lines in Fig. 12a) and b), the cast specimen and the specimen in condition (A-v) show strain distribution in several directions. This is because the compressive stress is mainly applied in this region, where the stress distribution is localized in the split tensile test.

Condition (A-p) shows a smaller strain than the cast specimen and condition (A-v). In addition, the strain is concentrated at the layer interface. This indicates that the layer interface is weak and leads to failure at a small strain compared to the cast specimen and the specimens in condition (A-v), resulted in decrease of tensile strength.

3.3. Results of bending test

3.3.1. Bending strength

Fig. 13 shows the bending strength obtained from the three-point bending test. Error bars indicate the Standard Deviation (SD) The bending strength of the xyx-printed and yxy-printed specimens are obtained from one sample each. However, the small variation in the bending strength of the x-printed and y-printed specimens means that the bending strength of the xyx-printed and yxy-printed specimens is reliable. Also, y-printed specimens show significantly smaller bending strength than the other printed specimens. In addition, the bending strength of the printed specimen is lower than that of the cast specimen, regardless of the print path.

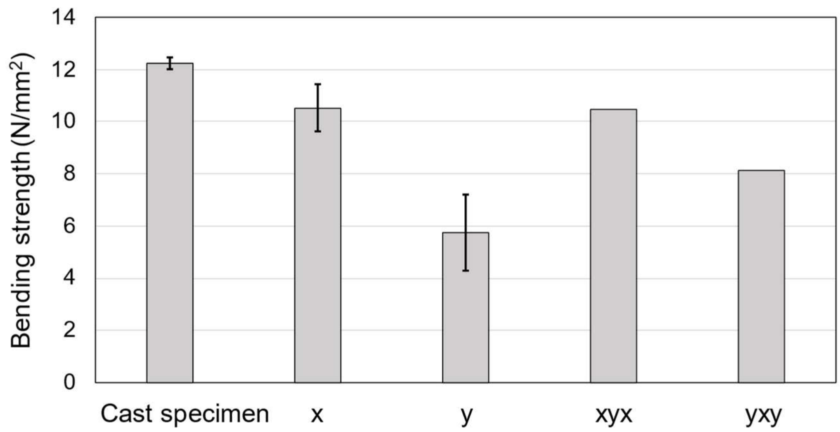

Fig. 13 Bending strength.

In the printed specimens, the bending strength of the y-printed specimen printed only in the short side direction is about 40% lower than that of the x-printed specimen printed only in the long side direction. This indicates anisotropy in the bending strength of printed specimens. Printing in the short side direction should be avoided as it significantly reduces the bending capacity. However, the bending strength of the xyx-printed specimen printed in the long-short-long side direction is almost the same as that of the x-printed specimen. In addition, the bending strength of the yxy-printed specimen printed in the short-long-short side direction increased by approximately 40% compared to that of the y-printed specimens. In other words, the decrease in bending strength of the printed specimen compared to that of the x-printed specimen is only approximately 20%. From the above-mentioned results, in the construction and the design of structures using 3DCP, it can be considered that the bending strength can be improved by printing some layers not only in the short side direction but also in the long side direction. Hence, it is important and necessary to evaluate the print path of this layer-by-layer combination for 3D printed concrete design in consideration of the bending fracture propagation behavior.

3.3.2. Fracture propagation

Fig. 14 shows the principal strain distribution at crack initiation (center) and 0.00025 seconds before (left) and after (right) cracking in bending test obtained by DIC. The bending strength value of each specimen is shown at the top left of each image.

In the cast specimen shown in Fig. 14a), no strain is clearly observed before crack initiation, and the crack propagates instantaneously in a straight line from the bottom surface to the top surface of the specimen. In other words, the cast specimen shows brittle bending failure behavior without localizing strain generation [59]. In contrast, all of the printed specimens show the strain development even before crack initiation in the bottom layer. Thus, it is considered that the printed specimen is relatively ductile while its flexural strength is lower than that of the cast specimen due to the layered structure, which allows a certain amount of strain generation and accumulation.

In the x-printed specimen, as shown in the center of Fig. 14b), a layered structure with layer interfaces and inter-filament voids can be observed. As shown in Fig. 14b), the cracks tortuously propagate in detoured line at the layer interface from the bottom surface to the top surface, changing the direction of crack propagation layer by layer.

In the y-printed specimen, filaments and inter-filament voids can be observed as shown in the center of Fig. 14c). The inter-filament voids are arranged irregularly due to tilting of the filaments caused by the print paths order with horizontal movement of nozzle. The principal strains are distributed in such directions as the layer interface connects the inter-filament voids located above and below each layer for the crack propagation path. As the result, the cracks propagate along the layer interface, as shown in Fig. 14c) right. In addition, the cracks occur at smaller strains than those of the cast specimen and the other printed specimens. In consequence, the bending strength of the y-printed specimens is much lower than that of the other specimens. The results also indicate that the layer interface and inter-filament void are the dominant fragile zones in the printed specimen for the starting point and the propagation zone of fracture.

In the xyx-printed specimen, large inter-filament voids are regularly aligned as shown in Fig. 14d). On the other hand, as in the cast specimen, the cracks propagate in a straight line from the bottom surface to the top surface so that the influence of inter-filament voids on the crack propagation is relatively small. As the result, The small effect of the inter-filament void on crack propagation caused equivalent bending strength to that of the cast and the x-printed specimens.

In the yxy-printed specimen, as shown in Fig. 14e), cracks propagate from the layer interface and inter-filament void on the bottom surface of the printed specimen, where the strains were concentrated. The bending strength of the yxy-printed specimen is improved over that of the y-printed specimen. In both printed specimens (y-printed and yxy-printed specimen), the strain propagates from the layer interface at the bottom of the specimen. The y-printed specimens have strain concentrated at the layer interface for all layers. In contrast, in the yxy-printed specimen which the middle layer is printed in the long-side direction, the cracks propagate in a straight line from the middle layer as in the xyx-printed specimen. Since the printing direction of the middle layer is different between the yxy-printed specimen and the y-printed specimen, the yxy-printed specimen displays higher bending strength.

The influence of layer interfaces and inter-filament voids on fracture propagation behavior is more dominant for those located on the printed specimen surface than for those located inside the printed specimen. In the xyx-printed specimen, the inter-filament voids are located inside the printed specimen and they work to block the crack propagation, thus having little effect on the mechanical properties of the printed specimen. In yxy-printed specimen, inter-filament voids are located on the bottom surface of the printed specimen, and these inter-filament voids are the starting point of fracture. As the result, the inter-filament voids in the yxy-printed specimen have a greater effect on the mechanical properties of the printed specimens than those in the xyx-printed specimen. Also, the bending strength of the yxy-printed specimen is smaller than that of the xyx-printed specimen. Therefore, the arrangement of the layer interface and inter-filament void is an important information in modeling the mechanical behavior of printed specimens, and their properties need to be further investigated for designing large-scale member.

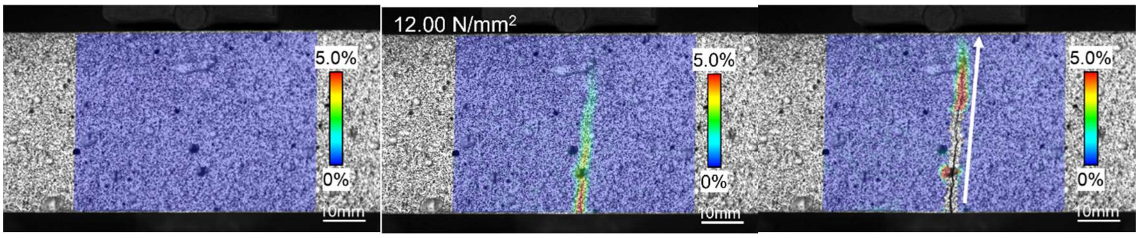

0.00025 sec before cracking | Cracking | 0.00025 sec after cracking

a) Cast specimen

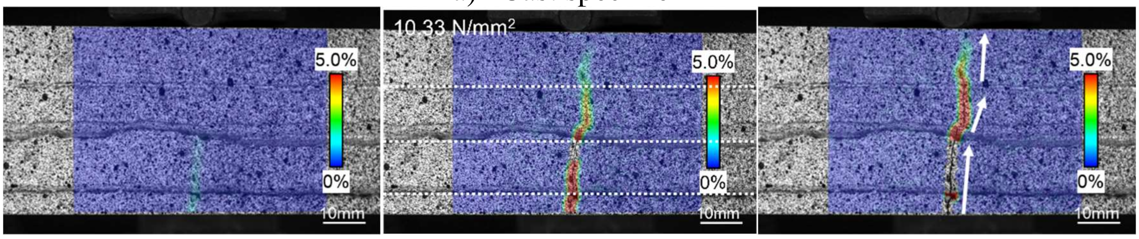

0.00025 sec before cracking | Cracking | 0.00025 sec after cracking

b) x-printed specimen

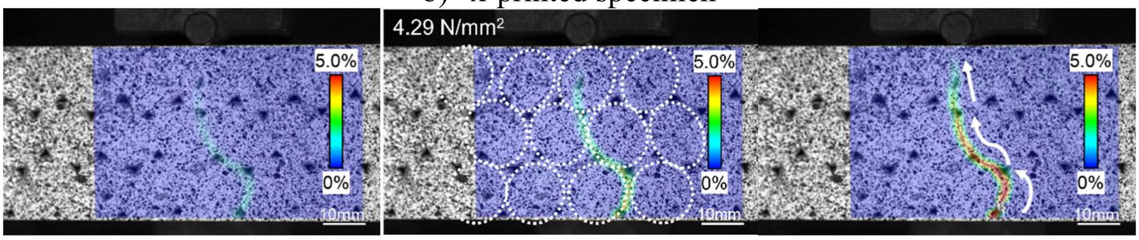

0.00025 sec before cracking | Cracking | 0.00025 sec after cracking

c) y-printed specimen

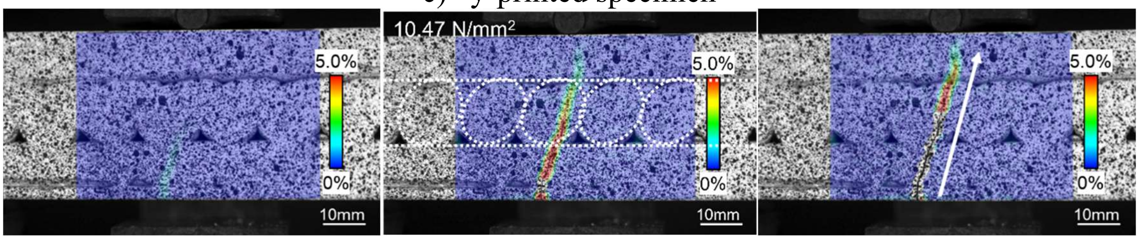

0.00025 sec before cracking | Cracking | 0.00025 sec after cracking

d) xyx-printed specimen

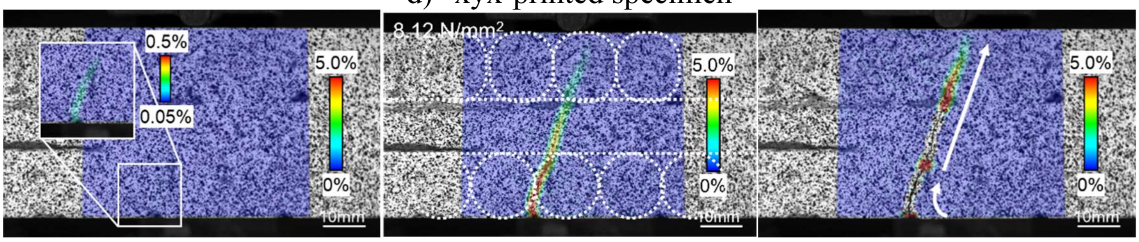

0.00025 sec before cracking | Cracking | 0.00025 sec after cracking

e) yxy-printed specimen

Fig. 14 Principal strain distribution by DIC.

4. Conclusion

In this paper, the fracture propagation behavior of 3D printed concrete under compression, tensile and bending stresses was evaluated to understand the effect of the print path on the mechanical properties. The following items are the findings in this study:

1. Compared to cast specimens, printed specimens have elongated intra-filament void shape due to the relationship between the material printing direction and the nozzle movement direction during the printing process.
2. When printed in only one direction, the inter-filament void structure is aligned in one direction. Meanwhile, when printed in orthogonal two-directions, the inter-filament void structure is formed in a complex lattice pattern.
3. Differences in inter-filament void formation and distribution affect the cracks that occur under compressive loading. When printed in one direction, the cracks propagate along with the layer interface with cracks connecting the inter-filament voids. On the other hand, when the specimen is printed in orthogonal two-directions, many micro cracks propagate from inter-filament voids distributed in a lattice pattern. Under compressive loading, the specimen printed in one direction shows anisotropic deformation perpendicular to the printing direction. In contrast, no anisotropy of deformation is observed when printed in orthogonal two-directions.
4. Under tensile stress, the tensile strength when loaded parallel to the printing direction is significantly lower than when loaded perpendicular to the printing direction. This indicates anisotropy in tensile strength. In the fracture propagation behavior under tensile stress, when the specimen is loaded parallel to the printing direction, the layer interface becomes a weaker zone than the hardened matrix where the tensile stress concentrates, causing the specimen to generate cracks at the layer interface.
5. Bending strength of printed specimens printed in the short side direction clearly decreased compared to those printed specimens printed in the long side direction under bending loading. Printed specimens with some of the layers printed in the long side direction show greater bending strength than printed in only short side direction. Depending on the combination of long and short side directions, the print path design potentially improves the structural performance of 3D printed concrete in bending strength. In the fracture propagation behavior under bending stress, the crack propagation direction changes at the layer interface of specimens printed in the long side direction. In the specimen printed in the short side direction, the cracks propagate along the layer interface between adjacent filaments, while connecting the inter-filament voids.

The results obtained in this paper showed that the layer interface and inter-filament void structure, which affect the fracture behavior of printed specimens, are affected by the printing process of the specimens, i.e., the print paths. It was also shown that it is possible to control the performance and mechanical properties of 3D printed concrete by controlling and designing the print path. This allows 3DCP to add new value to concrete structures in contrast to conventional cast construction.

CRediT authorship contribution statement

Kota NAKASE: Conceptualization, Methodology, Software, Writing - original draft. Katsufumi HASHIMOTO: Conceptualization, Funding acquisition, Resources, Writing – review & editing, Supervision. Takafumi SUGIYAMA: Writing – review & editing, Supervision. Katsuya KONO: Resources, Writing – review & editing, Supervision.

This research did not receive any specific grant from funding agencies in the public, commercial, or not-for-profit sectors.

References

[1] R.A. Buswell, W.R. Leal de Silva, S.Z. Jones, J. Dirrenberger, 3D printing using concrete extrusion: A roadmap for research, Cem Concr Res 112 (2018) 37–49. https://doi.org/10.1016/j.cemconres.2018.05.006.

[2] S. Lim, R.A. Buswell, T.T. Le, S.A. Austin, A.G.F. Gibb, T. Thorpe, Developments in construction-scale additive manufacturing processes, Autom Constr 21 (2012) 262–268. https://doi.org/10.1016/J.AUTCON.2011.06.010.

[3] G.H. Ahmed, N.H. Askandar, G.B. Jumaa, A review of largescale 3DCP: Material characteristics, mix design, printing process, and reinforcement strategies, Structures 43 (2022) 508–532. https://doi.org/10.1016/J.ISTRUC.2022.06.068.

[4] G.H. Ahmed, A review of “3D concrete printing”: Materials and process characterization, economic considerations and environmental sustainability, Journal of Building Engineering 66 (2023) 105863. https://doi.org/10.1016/j.jobe.2023.105863.

[5] T. Ding, J. Xiao, V. Mechtcherine, Microstructure and mechanical properties of interlayer regions in extrusion-based 3D printed concrete: A critical review, Cem Concr Compos 141 (2023) 105154. https://doi.org/10.1016/J.CEMCONCOMP.2023.105154.

[6] ASTM Standard F2792-12a, Standard Terminology for Additive Manufacturing Technologies, 2012.

[7] R.A. Buswell, W.R.L. da Silva, F.P. Bos, H.R. Schipper, D. Lowke, N. Hack, H. Kloft, V. Mechtcherine, T. Wangler, N. Roussel, A process classification framework for defining and describing Digital Fabrication with Concrete, Cem Concr Res 134 (2020) 106068. https://doi.org/10.1016/J.CEMCONRES.2020.106068.

[8] V. Mechtcherine, F.P. Bos, A. Perrot, W.R.L. da Silva, V.N. Nerella, S. Fataei, R.J.M. Wolfs, M. Sonebi, N. Roussel, Extrusion-based additive manufacturing with cement-based materials – Production steps, processes, and their underlying physics: A review, Cem Concr Res 132 (2020) 106037. https://doi.org/10.1016/J.CEMCONRES.2020.106037.

[9] G. De Schutter, K. Lesage, V. Mechtcherine, V.N. Nerella, G. Habert, I. Agusti-Juan, Vision of 3D printing with concrete — Technical, economic and environmental potentials, Cem Concr Res 112 (2018) 25–36. https://doi.org/10.1016/j.cemconres.2018.06.001.

[10] S. Bhattacherjee, A.S. Basavaraj, A. V. Rahul, M. Santhanam, R. Gettu, B. Panda, E. Schlangen, Y. Chen, O. Copuroglu, G. Ma, L. Wang, M.A. Basit Beigh, V. Mechtcherine, Sustainable materials for 3D concrete printing, Cem Concr Compos 122 (2021). https://doi.org/10.1016/j.cemconcomp.2021.104156.

[11] B. Panda, S.C. Paul, L.J. Hui, Y.W.D. Tay, M.J. Tan, Additive manufacturing of geopolymer for sustainable built environment, J Clean Prod 167 (2017) 281–288. https://doi.org/10.1016/J.JCLEPRO.2017.08.165.

[12] S.A. Khan, M. Koç, S.G. Al-Ghamdi, Sustainability assessment, potentials and challenges of 3D printed concrete structures: A systematic review for built environmental applications, J Clean Prod 303 (2021). https://doi.org/10.1016/j.jclepro.2021.127027.

[13] A. Paolini, S. Kollmannsberger, E. Rank, Additive manufacturing in construction: A review on processes, applications, and digital planning methods, Addit Manuf 30 (2019) 100894. https://doi.org/10.1016/J.ADDMA.2019.100894.

[14] P. Wu, J. Wang, X. Wang, A critical review of the use of 3-D printing in the construction industry, Autom Constr 68 (2016) 21–31. https://doi.org/10.1016/j.autcon.2016.04.005.

[15] Z. Geng, W. She, W. Zuo, K. Lyu, H. Pan, Y. Zhang, C. Miao, Layer-interface properties in 3D printed concrete: Dual hierarchical structure and micromechanical characterization, Cem Concr Res 138 (2020) 106220. https://doi.org/10.1016/J.CEMCONRES.2020.106220.

[16] T.T. Le, S.A. Austin, S. Lim, R.A. Buswell, R. Law, A.G.F. Gibb, T. Thorpe, Hardened properties of high-performance printing concrete, Cem Concr Res 42 (2012) 558–566. https://doi.org/10.1016/j.cemconres.2011.12.003.

[17] G. Ye, H. Bi, Y. Hu, Compression behaviors of 3D printed pyramidal lattice truss composite structures, Compos Struct 233 (2020) 111706. https://doi.org/10.1016/J.COMPSTRUCT.2019.111706.

[18] T.T. Le, S.A. Austin, S. Lim, R.A. Buswell, A.G.F. Gibb, T. Thorpe, Mix design and fresh properties for high-performance printing concrete, Materials and Structures/Materiaux et Constructions 45 (2012) 1221–1232. https://doi.org/10.1617/s11527-012-9828-z.

[19] Y.W.D. Tay, Y. Qian, M.J. Tan, Printability region for 3D concrete printing using slump and slump flow test, Compos B Eng 174 (2019) 106968. https://doi.org/10.1016/J.COMPOSITESB.2019.106968.

[20] A. V. Rahul, M. Santhanam, H. Meena, Z. Ghani, 3D printable concrete: Mixture design and test methods, Cem Concr Compos 97 (2019) 13–23. https://doi.org/10.1016/J.CEMCONCOMP.2018.12.014.

[21] N. Roussel, Rheological requirements for printable concretes, Cem Concr Res 112 (2018) 76–85. https://doi.org/10.1016/J.CEMCONRES.2018.04.005.

[22] S. Ketel, G. Falzone, B. Wang, N. Washburn, G. Sant, A printability index for linking slurry rheology to the geometrical attributes of 3D-printed components, Cem Concr Compos 101 (2019) 32–43. https://doi.org/10.1016/J.CEMCONCOMP.2018.03.022.

[23] Y.C. Wu, M. Li, Effects of Early-Age rheology and printing time interval on Late-Age fracture characteristics of 3D printed concrete, Constr Build Mater 351 (2022) 128559. https://doi.org/10.1016/J.CONBUILDMAT.2022.128559.

[24] R.J.M. Wolfs, T.A.M. Salet, N. Roussel, Filament geometry control in extrusion-based additive manufacturing of concrete: The good, the bad and the ugly, Cem Concr Res 150 (2021) 106615. https://doi.org/10.1016/J.CEMCONRES.2021.106615.

[25] N. Zhang, J. Sanjayan, Extrusion nozzle design and print parameter selections for 3D concrete printing, Cem Concr Compos 137 (2023) 104939. https://doi.org/10.1016/J.CEMCONCOMP.2023.104939.

[26] R.J.M. Wolfs, F.P. Bos, T.A.M. Salet, Hardened properties of 3D printed concrete: The influence of process parameters on interlayer adhesion, Cem Concr Res 119 (2019) 132–140. https://doi.org/10.1016/J.CEMCONRES.2019.02.017.

[27] Q. Yuan, Z. Xie, H. Yao, T. Huang, Z. Li, X. Zheng, Effect of polyacrylamide on the workability and interlayer interface properties of 3D printed cementitious materials, Journal of Materials Research and Technology 19 (2022) 3394–3405. https://doi.org/10.1016/j.jmrt.2022.06.093.

[28] H. Lee, J.H.J. Kim, J.H. Moon, W.W. Kim, E.A. Seo, Correlation between pore characteristics and tensile bond strength of additive manufactured mortar using X-ray computed tomography, Constr Build Mater 226 (2019) 712–720. https://doi.org/10.1016/j.conbuildmat.2019.07.161.

[29] H. Kloft, H.W. Krauss, N. Hack, E. Herrmann, S. Neudecker, P.A. Varady, D. Lowke, Influence of process parameters on the interlayer bond strength of concrete elements additive by Shotcrete 3D Printing (SC3DP), Cem Concr Res 134 (2020) 106078. https://doi.org/10.1016/J.CEMCONRES.2020.106078.

[30] J. Kruger, A. du Plessis, G. van Zijl, An investigation into the porosity of extrusion-based 3D printed concrete, Addit Manuf 37 (2021) 101740. https://doi.org/10.1016/J.ADDMA.2020.101740.

[31] H. Kloft, H.W. Krauss, N. Hack, E. Herrmann, S. Neudecker, P.A. Varady, D. Lowke, Influence of process parameters on the interlayer bond strength of concrete elements additive manufactured by Shotcrete 3D Printing (SC3DP), Cem Concr Res 134 (2020) 106078. https://doi.org/10.1016/J.CEMCONRES.2020.106078.

[32] T. Marchment, J. Sanjayan, M. Xia, Method of enhancing interlayer bond strength in construction scale 3D printing with mortar by effective bond area amplification, Mater Des 169 (2019). https://doi.org/10.1016/j.matdes.2019.107684.

[33] L. He, H. Li, W.T. Chow, B. Zeng, Y. Qian, Increasing the interlayer strength of 3D printed concrete with tooth-like interface: An experimental and theoretical investigation, Mater Des 223 (2022) 111117. https://doi.org/10.1016/J.MATDES.2022.111117.

[34] B. Panda, S. Chandra Paul, M. Jen Tan, Anisotropic mechanical performance of 3D printed fiber reinforced sustainable construction material, Mater Lett 209 (2017) 146–149. https://doi.org/10.1016/J.MATLET.2017.07.123.

[35] J. Xiao, H. Liu, T. Ding, Finite element analysis on the anisotropic behavior of 3D printed concrete under compression and flexure, Addit Manuf 39 (2021) 101712. https://doi.org/10.1016/J.ADDMA.2020.101712.
[36] H. Liu, C. Liu, G. Bai, Y. Wu, C. He, R. Zhang, Y. Wang, Influence of pore defects on the hardened properties of 3D printed concrete with coarse aggregate, Addit Manuf 55 (2022) 102843. https://doi.org/10.1016/J.ADDMA.2022.102843.
[37] S. Skibicki, R. Dvořák, L. Pazdera, L. Topolář, D. Kocáb, M. Alexa, K. Cendrowski, M. Hoffmann, Anisotropic Mechanical Properties of 3d Printed Mortar by Standard Flexural and Compression Test and Acoustic Emission. Available at SSRN: https://ssrn.com/abstract=4543414. or http://dx.doi.org/10.2139/ssrn.4543414.
[38] Q. Lyu, P. Dai, A. Chen, Sandwich-structured porous concrete manufactured by mortar-extrusion and aggregate-bed 3D printing, Constr Build Mater 392 (2023) 131909. https://doi.org/10.1016/J.CONBUILDMAT.2023.131909.
[39] G. Tanapornraweekit, P. Jiramarootapong, S. Paudel, S. Tangtermsirikul, C. Snguanyat, Experimental and numerical investigation of 3D-printed mortar walls under uniform axial compression, Constr Build Mater 360 (2022) 129552. https://doi.org/10.1016/J.CONBUILDMAT.2022.129552.
[40] X. Sun, M. Mazur, C.T. Cheng, A review of void reduction strategies in material extrusion-based additive manufacturing, Addit Manuf 67 (2023) 103463. https://doi.org/10.1016/J.ADDMA.2023.103463.
[41] Z. Pan, D. Si, J. Tao, J. Xiao, Compressive behavior of 3D printed concrete with different printing paths and concrete ages, Case Studies in Construction Materials 18 (2023) e01949. https://doi.org/10.1016/J.CSCM.2023.E01949.
[42] D. Heras Murcia, M. Genedy, M.M. Reda Taha, Examining the significance of infill printing pattern on the anisotropy of 3D printed concrete, Constr Build Mater 262 (2020) 120559. https://doi.org/10.1016/J.CONBUILDMAT.2020.120559.
[43] J.G. Yue, D.E. Beskos, C. Feng, K. Wu, Hardened fracture characteristics of printed concrete using acoustic emission monitoring technique, Constr Build Mater 361 (2022) 129684. https://doi.org/10.1016/J.CONBUILDMAT.2022.129684.
[44] L. Wang, H. Jiang, Z. Li, G. Ma, Mechanical behaviors of 3D printed lightweight concrete structure with hollow section, Archives of Civil and Mechanical Engineering 20 (2020). https://doi.org/10.1007/s43452-020-00017-1.
[45] K.K. Yang, J.H. Zhu, C. Wang, D.S. Jia, L.L. Song, W.H. Zhang, Experimental validation of 3D printed material behaviors and their influence on the structural topology design, Comput Mech 61 (2018) 581–598. https://doi.org/10.1007/s00466-018-1537-1.

[46] Ç. Yalçınkaya, O. Çopuroğlu, Hydration heat, strength and microstructure characteristics of UHPC containing blast furnace slag, Journal of Building Engineering 34 (2021) 101915. https://doi.org/10.1016/J.JOBE.2020.101915.

[47] M. van den Heever, A. du Plessis, J. Kruger, G. van Zijl, Evaluating the effects of porosity on the mechanical properties of extrusion-based 3D printed concrete, Cem Concr Res 153 (2022) 106695. https://doi.org/10.1016/J.CEMCONRES.2021.106695.

[48] B. Panda, S.C. Paul, N.A.N. Mohamed, Y.W.D. Tay, M.J. Tan, Measurement of tensile bond strength of 3D printed geopolymer mortar, Measurement 113 (2018) 108–116. https://doi.org/10.1016/J.MEASUREMENT.2017.08.051.

[49] T. Sugiyama, M.A.B. Promentilla, Advancing concrete durability research through X-ray computed tomography, Journal of Advanced Concrete Technology 19 (2021) 730–755. https://doi.org/10.3151/jact.19.730.

[50] Y. Tan, T. Sugiyama, K. Hashimoto, Evaluation of transport properties of deteriorated concrete due to calcium leaching with coupled CT image analysis and random walk simulation, Constr Build Mater 369 (2023) 130526. https://doi.org/10.1016/J.CONBUILDMAT.2023.130526.

[51] Miyagawa. Y, Shibayama. A, Kanazawa. K, Displacement Distribution Measurement of Specimens and Real Structure with 3D scanner, Concrete Journal 60 (2022) 796–802.

[52] S. Yamamoto, H. Ogura, H. Abe, R. Kikuchi, Development and Practical Application of 3D Printing Technology for Construction, Concrete Journal 59 (2021) 655–660.

[53] T.C. Chu, W.F. Ranson, M.A. Sutton, Applications of digital-image-correlation techniques to experimental mechanics, Exp Mech 25 (1985) 232–244. https://doi.org/10.1007/BF02325092.

[54] S.C. Kou, C.S. Poon, M. Etxeberria, Influence of recycled aggregates on long term mechanical properties and pore size distribution of concrete, Cem Concr Compos 33 (2011) 286–291. https://doi.org/10.1016/J.CEMCONCOMP.2010.10.003.

[55] Y. Li, Y. Su, K.H. Tan, X. Zheng, J. Sheng, Pore structure and splitting tensile strength of hybrid Basalt–Polypropylene fiber reinforced concrete subjected to carbonation, Constr Build Mater 297 (2021) 123779. https://doi.org/10.1016/J.CONBUILDMAT.2021.123779.

[56] M. Rezanezhad, S.A. Lajevardi, S. Karimpouli, Effects of pore-crack relative location on crack propagation in porous media using XFEM method, Theoretical and Applied Fracture Mechanics 103 (2019) 102241. https://doi.org/10.1016/J.TAFMEC.2019.102241.

[57] W. Tian, N. Han, Pore characteristics (>0.1 mm) of non-air entrained concrete destroyed by freeze-thaw cycles based on CT scanning and 3D printing, Cold Reg Sci Technol 151 (2018) 314–322. https://doi.org/10.1016/J.COLDREGIONS.2018.03.027.

[58] Y. Zhang, H. Qiao, R. Qian, C. Xue, Q. Feng, L. Su, Y. Zhang, G. Liu, H. Du, Relationship between water transport behaviour and interlayer voids of 3D printed concrete, Constr Build Mater 326 (2022) 126731. https://doi.org/10.1016/J.CONBUILDMAT.2022.126731.

[59] A.A. Jhatial, S. Sohu, N.-K. Bhatti, M.T. Lakhiar, R. Oad, Effect of steel fibres on the compressive and flexural strength of concrete, International Journal of ADVANCED AND APPLIED SCIENCES 5 (2018) 16–21. https://doi.org/10.21833/ijaas.2018.10.003.